Discontinuous Galerkin Time-Domain Method in Computational Electrodynamic Scattering Problems

Tiago Vilela Lima Amorim
Graduate Program in Electrical Engineering
Federal University of Minas Gerais
Belo Horizonte, Brazil
tiagovla@ufmg.br

Elson José da Silva
Department of Electrical Engineering
Federal University of Minas Gerais
Belo Horizonte, Brazil
elson@cpdee.ufmg.br

Fernando José da Silva Moreira
Department of Electronics Engineering
Federal University of Minas Gerais
Belo Horizonte, Brazil
fernandomoreira@ufmg.br

***Abstract*—A discontinuous Galerkin method is presented to accurately calculate electromagnetic scattering from perfect electric conductor and dielectric objects in the time-domain. In order to validate the formulation therein, two-dimensional canonical scattering problems were solved. The Fourier transform of the time-domain solution was compared to the frequency-domain analytical solution at a given frequency.**

***Keywords*—discontinuous galerkin, scattering, electromagnetism**

I. Introduction

Among the various numerical techniques applied to Computational Electrodynamics (CEM), the Discontinuous Galerkin Time-Domain (DGTD) has drawn considerable attention for transient analysis in the past decades [1]–[3].

As a combination of the Finite Volume Method (FVM) [4], [5] and the Finite Element Method (FEM) [6], [7], the DGTD method inherits the advantages of obtaining highly accurate results and handling complex geometry structures at an affordable computational cost.

The Discontinuous Galerkin (DG) method can be seen as a variant of the traditional FEM. The whole computational domain is partitioned into a set of elements forming an unstructured mesh, and the physical fields are expanded in terms of basis functions on each element. The primary dissimilarity to FEM is that these basis functions are confined to their respective elements; hence the fields are continuous inside elements and can be discontinuous at the interface of adjoining elements. The concept of numerical flux, borrowed from the FVM, is used to reintroduce the coupling between neighboring elements and produce a unique global solution. A semi-discrete form in which the position dependence is already discretized is obtained, and the remaining time dependence can therefore be carried out with an explicit time integration marching scheme, such as the leap-frog scheme [8] or the Runge-Kutta scheme [9], making the DG method highly competitive with the Finite-Difference Time-Domain (FDTD) [10] method.

As a consequence of its geometry flexibility, high accuracy, and explicit scheme, the DGTD method is exceptionally suitable for CEM transient simulations. The performance can be improved with proper techniques, such as local time-step schemes [11], dynamic hp-adaptation strategies [12], non conformal meshes and curved elements [1]. Furthermore, parallel algorithms developed to solve large-scale realistic problems using MPI parallelization with multicore CPU [13] and Compute Unified Device Architecture (CUDA) with GPU [14] can further improve the computational processing time.

The main concepts required to implement a DGTD formulation applied to CEM using nodal-basis functions are detailed in Section II. Additionally, a summary of the results used for validation is provided in Section III.

II. The Discontinuous Galerkin Method

Maxwell's curl equations for lossless isotropic linear media without sources [15] are defined as

$$\mu \frac{\partial \vec{\mathscr{H}}}{\partial t} = -\nabla \times \vec{\mathscr{E}}, \tag{1}$$

$$\epsilon \frac{\partial \vec{\mathscr{E}}}{\partial t} = \nabla \times \vec{\mathscr{H}}, \tag{2}$$

where $\vec{\mathscr{E}}$ and $\vec{\mathscr{H}}$ are the electric and magnetic fields in the time-domain, respectively. Moreover, ϵ and μ are the electric permittivity and the magnetic permeability, respectively.

In conservation form, the aforementioned equations become [16]

$$\mathcal{Q} \frac{\partial \vec{q}}{\partial t} + \nabla \cdot \mathcal{F} = 0, \tag{3}$$

where

$$\vec{q}(\vec{r},t) = \begin{bmatrix} \vec{\mathscr{H}}(\vec{r},t) \\ \vec{\mathscr{E}}(\vec{r},t) \end{bmatrix}, \qquad \mathcal{Q}(\vec{r},t) = \begin{bmatrix} \bar{\bar{\mu}}(\vec{r}) & 0 \\ 0 & \bar{\bar{\epsilon}}(\vec{r}) \end{bmatrix},$$

$$\mathcal{F}(\vec{q}) = \left[\mathcal{F}_1, \mathcal{F}_2, \mathcal{F}_3\right]^{\mathsf{T}}, \qquad \mathcal{F}_i(\vec{q}) = \begin{bmatrix} \vec{e}_i \times \vec{\mathscr{E}}(\vec{r},t) \\ -\vec{e}_i \times \vec{\mathscr{H}}(\vec{r},t) \end{bmatrix},$$

with $\mathcal{F}$ being the flux and $\vec{e}_i$ representing the three Cartesian unit vectors. Furthermore, $\vec{r}$ and t indicate the spacial position and time, respectively.

A. The Galerkin Method

Assuming that Ω^h is a tessellated finite region (bounded by $\partial\Omega^h$) of the physical domain Ω with K non-overlapping elements (Ω^k, bounded by $\partial\Omega_k^h$) where (1) and (2) are solved. Therefore

$$\Omega \approx \Omega_h = \bigcup_k^K \Omega_h^k. \tag{4}$$

Introducing a globally defined space $\mathcal{V}_h$ of test functions, ϕ_h, as $\mathcal{V}_h = \oplus_{k=1}^K \mathcal{V}_h^k$ where the locally defined spaces are defined as $\mathcal{V}_h^k = \text{span}\{\psi_n(\Omega_h^k)\}_{n=1}^N$. Considering that $\mathcal{V}_h$ is piecewise smooth over Ω_h, a member of this space is [1]

$$\begin{aligned}\phi_h^k(\vec{r},t) &= \sum_{n=1}^N \hat{\phi}_n^k(t)\cdot\psi_n(\vec{r}) \\ &= \sum_{n=1}^N \tilde{\phi}_n^k(\vec{r_n},t)\cdot l_n(\vec{r}) \quad \vec{r}\in\Omega^k,\end{aligned} \tag{5}$$

where l_n are the interpolating Lagrange nodal-basis which have the Kronecker delta property [3]. The relation between modal coefficients $\hat{\phi}_n^k(t)$ and nodal coefficients $\tilde{\phi}_n^k(\vec{r_n},t)$ are given by the Vandermonde matrix [1]. The modal-basis are usually chosen to be normalized monomials, while the interpolating positions $\vec{r}_n$ are spread in a Gauss-Lobatto alike distribution, usually obtained by the Warp&Blend method [1].

By applying the Galerkin testing and integration by parts over (3), for each element, the strong variational formulation of Maxwell's curl equations [3] can be derived as

$$\begin{aligned}&\int_{\Omega_h^k}\left[\mathcal{Q}\frac{\partial\vec{q}_h^k}{\partial t}+\nabla\cdot\mathcal{F}_h^k(\vec{q}_h^k)\right]\cdot l_i(\vec{r})\,d\Omega_h = \\ &\int_{\partial\Omega_h^k}\hat{n}\cdot\left[\mathcal{F}_h^k(\vec{q}_h^k)-\mathcal{F}^*(\vec{q}_h^k)\right]\cdot l_i(\vec{r})\,d\Omega_h \quad \forall l_i\in\mathcal{V}_h^k,\end{aligned} \tag{6}$$

where $\hat{n}$ is the outward unit vector normal to the boundary surface $\partial\Omega_h^k$ and $\mathcal{F}_h^k - \mathcal{F}^*$ are termed as the numerical flux difference used for information exchange.

Within each element, using the Galerkin approach, the physical fields $\vec{\mathscr{E}}(\vec{r},t)$ and $\vec{\mathscr{H}}(\vec{r},t)$ are approximated by a projection over the same testing set of nodal-basis functions:

$$\mathscr{E}_h^k(\vec{r},t) = \sum_{j=1}^N \tilde{E}_j^k(\vec{r}_j,t)\cdot l_j(\vec{r}) \qquad \vec{r}\in\Omega_h^k, \tag{7}$$

$$\mathscr{H}_h^k(\vec{r},t) = \sum_{j=1}^N \tilde{H}_j^k(\vec{r}_j,t)\cdot l_j(\vec{r}) \qquad \vec{r}\in\Omega_h^k, \tag{8}$$

After replacing Eqs. (7) and (8) into Eq. (6), assuming that $\mathcal{Q}$ in Eq. (3) is constant within each element for simplicity, the occurring integrals simplify to

$$\mathcal{M}_{ij}^k = \int_{\Omega_h^k} l_i(\vec{r})\cdot l_j(\vec{r})\,d\Omega_h, \tag{9}$$

$$\mathcal{S}_{ij,s}^k = \int_{\Omega_h^k} l_i(\vec{r})\cdot\frac{\partial l_j(\vec{r})}{\partial s}\,d\Omega_h \quad s=x,y,z, \tag{10}$$

$$\mathcal{F}_{ij,f}^k = \int_{\partial\Omega_h^k} l_i(\vec{r})\cdot l_j(\vec{r})\,d\Omega_h. \tag{11}$$

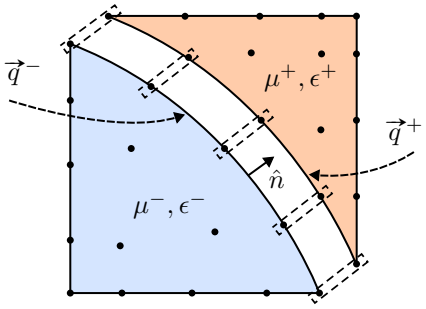

Fig. 1. Notation used for the definition of numerical fluxes. The blue element color represents the local element while the orange color represents a neighboring element.

where $\mathcal{M}^k$ is the mass matrix, $\mathcal{S}_s^k$ is the stiffness matrix along s and the face mass matrix $\mathcal{F}_f^k$. Isolating the time-derivatives one obtains

$$\frac{\partial\tilde{E}^k}{\partial t} = \frac{\left(\mathcal{M}^k\right)^{-1}}{\epsilon^k}\cdot\left[\mathcal{S}^k\times\tilde{H}^k+\mathcal{F}_f^k\cdot\left(\hat{n}\cdot\left[\mathcal{F}_E^k-\mathcal{F}_E^*\right]\right)\right], \tag{12}$$

$$\frac{\partial\tilde{H}^k}{\partial t} = \frac{\left(\mathcal{M}^k\right)^{-1}}{\mu^k}\cdot\left[-\mathcal{S}^k\times\tilde{E}^k+\mathcal{F}_f^k\cdot\left(\hat{n}\cdot\left[\mathcal{F}_H^k-\mathcal{F}_H^*\right]\right)\right], \tag{13}$$

where $\mathcal{S}^k = \left[\mathcal{S}_x^k,\mathcal{S}_y^k,\mathcal{S}_z^k\right]^\intercal$, and $\mathcal{F}_E$ and $\mathcal{F}_H$ are the fluxes related to the electric and magnetic field, respectively. The full details of this notation can be found in [3].

B. Numerical Flux

The numerical flux for the linear case can be derived by solving a Riemann problem with Rankine-Hugoniot jump conditions [1] along a normal $\hat{n}$. Therefore, the flux difference is commonly defined as

$$\begin{aligned}\hat{n}\cdot(\mathcal{F}-\mathcal{F}^*) &= \hat{n}\cdot\begin{pmatrix}\mathcal{F}_E-\mathcal{F}_E^*\\ \mathcal{F}_H-\mathcal{F}_H^*\end{pmatrix} \\ &= \begin{pmatrix}-\dfrac{1}{\{\{Z\}\}}\dfrac{\hat{n}\times(Z^+[\vec{H}]+\alpha\hat{n}\times[\vec{E}])}{2}\\ \dfrac{1}{\{\{Y\}\}}\dfrac{\hat{n}\times(Y^+[\vec{E}]+\alpha\hat{n}\times[\vec{H}])}{2}\end{pmatrix},\end{aligned} \tag{14}$$

where

$$[u]=u^- - u^+, \quad \{\{u\}\}=\frac{u^-+u^+}{2}, \quad Z^\pm=\frac{1}{Y^\pm}=\sqrt{\frac{\mu^\pm}{\epsilon^\pm}}.$$

In this notation, "$-$" represents the local element while "$+$" represents the neighboring element, shown in Fig. 1. The upwind parameter $\alpha\in[0,1]$ ensures that the scheme is stable and convergent. Setting $\alpha=1$ represents the pure upwind flux, whereas the central flux can be recovered with $\alpha=0$.

C. Boundary Conditions

Perfect Electric Conductors (PEC) and Perfect Magnetic Conductors (PMC) reflect all incident radiation while Silver-Müller boundary conditions can partially absorb outgoing

radiation, mimicking an infinite computational domain. Common boundary conditions are naturally imposed [3] and are summarized in Tab. I.

TABLE I
FIELD DIFFERENCES FOR COMMONLY USED BOUNDARY CONDITIONS.

Boundary Condition	$[\mathscr{E}]$	$[\mathscr{H}]$
Perfect Electric Conductor (PEC)	$2\mathscr{E}^-$	0
Perfect Magnetic Conductor (PMC)	0	$2\mathscr{H}^-$
First Order Absorving (Silver Müller)	$2\mathscr{E}^-$	$2\mathscr{H}^-$

D. Perfect Matched Layers

Perfect Matched Layers (PMLs) have many advantages over Absorbing Boundary Conditions (ABCs) including being independent of frequency, wave polarization, and angle of incidence. The general time-harmonic Maxwell's equations within frequency domain in the Uniaxial Perfect Matching Layer (UPML) medium [17] are given by

$$\nabla \times \vec{H} = \quad j\omega\bar{\bar{\epsilon}}\vec{E}, \tag{15}$$
$$\nabla \times \vec{E} = -j\omega\bar{\bar{\mu}}\vec{H}, \tag{16}$$

where

$$\bar{\bar{\epsilon}} \equiv \bar{\bar{\Lambda}}\epsilon, \qquad \bar{\bar{\mu}} \equiv \bar{\bar{\Lambda}}\mu, \qquad \bar{\bar{\Lambda}} \equiv \begin{pmatrix} \frac{s_y s_z}{s_x} & 0 & 0 \\ 0 & \frac{s_x s_z}{s_y} & 0 \\ 0 & 0 & \frac{s_x s_y}{s_z} \end{pmatrix},$$

given that the UPML parameters for $i = x, y, z$ are

$$s_i = k_i + \frac{\sigma_i}{j\omega\epsilon_0}. \tag{17}$$

Directly implementing (15) and (16) leads to a convolution between the tensor coefficients and the electromagnetic fields which is computationally intensive. A better approach is to define constitutive relationships to decouple the frequency terms, specifically

$$\vec{D} = \bar{\bar{s}}\epsilon\vec{E}, \tag{18}$$
$$\vec{B} = \bar{\bar{s}}\mu\vec{H}, \tag{19}$$

with

$$\bar{\bar{s}} \equiv \begin{pmatrix} \frac{s_z}{s_x} & 0 & 0 \\ 0 & \frac{s_x}{s_y} & 0 \\ 0 & 0 & \frac{s_y}{s_z} \end{pmatrix}.$$

Using the constitutive relationships as an intermediary stage and then applying the inverse Fourier transform, precisely the identity $j\omega f(\omega) = \partial/\partial t f(t)$, yields a system of time-domain differential equations [18]. This system can be straightforwardly implemented into the DG method [3].

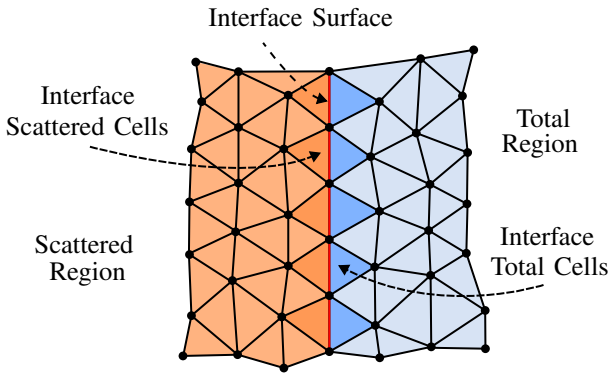

Fig. 2. Scattered field region (orange) and total field region (blue). The elements that need to be modified are marked in darker colors.

E. Sources

Based on the Huygen's principle, it is possible to split the computational domain into two regions: the Total Field Region (TFR) and the Scattered Field Region (SFR). This technique, known as the Total-Field/Scattered-Field (TF/SF) formulation [17], is widely used in the FDTD method. It relies on the linearity of Maxwell's equations and the known scattering relation

$$\vec{q}_{\text{tot}}(\vec{r}, t) = \vec{q}_{\text{inc}}(\vec{r}, t) + \vec{q}_{\text{scat}}(\vec{r}, t). \tag{20}$$

The subscripts "tot", "scat", and "inc" indicate the total, scattered and incident, i.e., physical fields, respectively. The incident field is a known analytical expression, e.g., a plane wave. An illustration of the scheme is shown in Fig. 2.

Due to linearity, equation (3) is still valid in the TFR and SFR. Hence, the equations

$$\mathcal{Q}\frac{\partial \vec{q}_{\text{tot}}}{\partial t} + \nabla \cdot \mathcal{F}(\vec{q}_{\text{tot}}) = 0, \tag{21}$$
$$\mathcal{Q}\frac{\partial \vec{q}_{\text{scat}}}{\partial t} + \nabla \cdot \mathcal{F}(\vec{q}_{\text{scat}}) = 0, \tag{22}$$

are solved in their respective domains. The field differences are

$$[\vec{q}_{\text{tot}}] = \vec{q}^{-}_{\text{tot}} - \vec{q}^{+}_{\text{tot}}, \tag{23}$$
$$[\vec{q}_{\text{scat}}] = \vec{q}^{-}_{\text{scat}} - \vec{q}^{+}_{\text{scat}}. \tag{24}$$

As long as the local element is within TFR or SFR, the evaluation is straightforward. The only change happens at interface elements sharing a face with the TF/SF interface surface. If the local element is in the TFR, the field difference is updated to

$$[\vec{q}]_{\text{tot}} = \vec{q}^{-}_{\text{tot}} - \vec{q}^{+}_{\text{scat}} - \vec{q}_{\text{inc}}, \tag{25}$$

while if the local element is within the SFR

$$[\vec{q}]_{\text{scat}} = \vec{q}^{-}_{\text{scat}} - \vec{q}^{+}_{\text{tot}} + \vec{q}_{\text{inc}}. \tag{26}$$

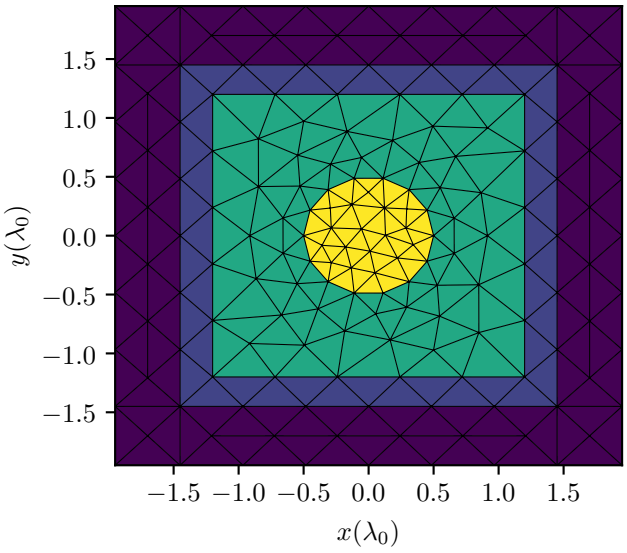

Fig. 3. Geometry of the scattering problem analyzed. It is shown the cylinder in yellow, the TFR in green, the SFR in blue and the PML in purple which is also within the SFR.

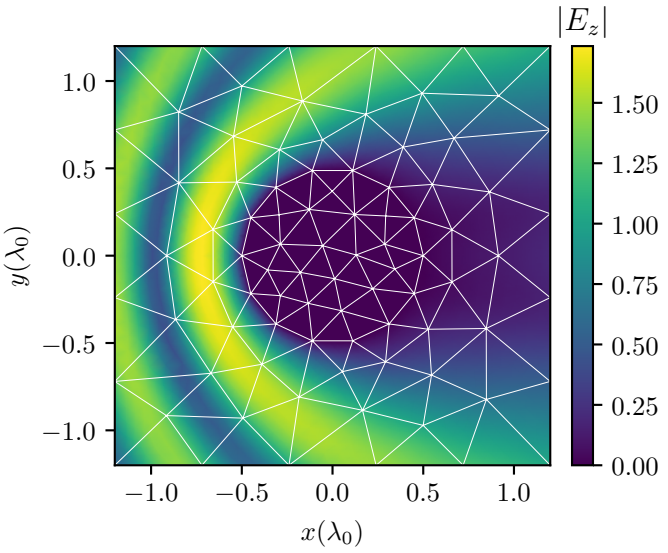

Fig. 4. Scattering by a PEC cylinder at 300MHz with 8th order elements.

III. Numerical Results

In order to validate the formulation, the two-dimensional canonical problems of the scattering of a TMz wave by a PEC and dielectric cylinders in free-space were simulated. Since a simulation needs to finish in a finite amount of time, and given that it is important for the TF/SF formulation that at $t = 0$ the electromagnetic fields are sufficiently close to zero for all positions $\vec{r}$ within the total-field region as well for large values of t [3], the cosine-modulated Gaussian waveform [19] was employed to represent the incident field:

$$g(t) = \cos(2\pi f_c t) \exp\left(-t^2/\tau^2\right), \tag{27}$$

with a center frequency $f_c = 300$MHz (free-space wavelength $\lambda_0 \approx 1$m) and a time constant $\tau = 1/600 \cdot 10^{-6}$ s. The incident field was chosen to have TMz polarization and propagation in the positive $\hat{x}$ direction [19]:

$$\vec{E}_{\text{inc}}(\vec{r}, t) = g(t - \frac{1}{c_0}\hat{x} \cdot \vec{r})\hat{z}, \tag{28}$$

$$\vec{H}_{\text{inc}}(\vec{r}, t) = \frac{1}{\eta_0}\hat{x} \times \vec{E}_{\text{inc}}, \tag{29}$$

where c_0 is the speed of light in free-space and η_0 is the free-space impedance.

The geometry of the scattering problem containing 308 triangular elements is shown in Fig. 3. The cylinder's radius corresponds to $0.5\lambda_0$, the TFR has dimensions $2.4\lambda_0 \times 2.4\lambda_0$, the SFR's width is $0.25\lambda_0$ and the PML's width is $0.50\lambda_0$.

At the outer boundary of the PML, a first order ABC was used, while the PML's parameters were manually tuned to $k_i = 1$ and $\sigma_i = 100$ for $i = x, y, z$.

The simulation was carried out for $10/300 \cdot 10^{-6}$s using a 5 stage 4th order Runge-Kutta integration scheme [1]. Then, the Fourier transform was taken. The module $|E_z|$ normalized by $|E_{z,\text{inc}}|$ at 300MHz in the TFR is shown in Figs. 4 and 5 for the PEC cylinder and the dielectric cylinder with relative electric permittivity $\epsilon_r = 2$, respectively.

The error analysis is shown in Tab. II using the relative error

$$\text{Error} = \sum_{n=1}^{N} \frac{|E_{\text{analytical}} - E_{\text{numerical}}|}{N}, \tag{30}$$

for different element orders with N being the number of Degrees of Freedom (DoFs). Here, the analytical solutions [20] were compared to the calculated ones inside the TFR.

TABLE II
Electric Field Error Analysis

Order	DoFs	Error (PEC)	Error (Dielectric)
5	6468	$4.11 \cdot 10^{-3}$	$1.46 \cdot 10^{-2}$
6	8624	$3.37 \cdot 10^{-3}$	$1.27 \cdot 10^{-2}$
8	13860	$2.41 \cdot 10^{-3}$	$0.99 \cdot 10^{-2}$

The normalized average processing time is shown in Tab. III where the number of timesteps is calculated based on [1].

TABLE III
Processing Time Analysis

Order	#Timesteps	Processing Time (PEC)
5	1202	100%
6	1571	167%
8	13860	533%

The error analysis shows that the order of the element used and their respective errors are inversely proportional since a higher-order polynomial can better approximate the solution. It can also be noted that increasing the order of the element can dramatically increase the number of DoFs and consequently lead to growth in processing time.

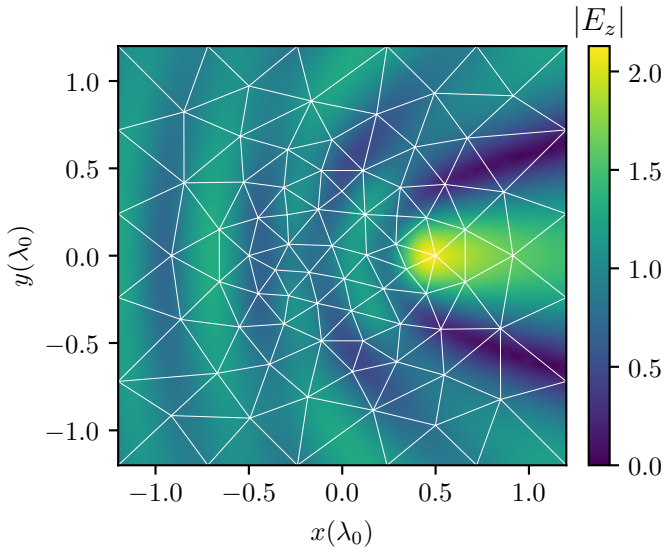

Fig. 5. Scattering by a dielectric cylinder at 300MHz with 8th order elements.

IV. Conclusion

This work presented a DGDT formulation applied to computational electrodynamic scattering problems. The canonical two-dimensional scattering of a TMz wave by a cylinder was simulated. The Fourier transform of the time-domain solution was compared to the frequency-domain analytical solutions at a given frequency. In conclusion, the DGDT method can produce accurate results in its traditional form and can further be optimized using proper techniques.

Acknowledgment

This work was partially supported by the Brazilian agencies CAPES and CNPq.

References

[1] J. S. Hesthaven and T. Warburton, *Nodal Discontinuous Galerkin Methods*, ser. Texts in Applied Mathematics, J. E. Marsden, L. Sirovich, and S. S. Antman, Eds. New York, NY: Springer New York, 2008, vol. 54.

[2] L. D. Angulo, J. Alvarez, M. F. Pantoja, S. G. Garcia, and A. R. Bretones, "Discontinuous galerkin time domain methods in computational electrodynamics: State of the art," p. 25.

[3] K. Busch, M. König, and J. Niegemann, "Discontinuous galerkin methods in nanophotonics," *Laser & Photonics Reviews*, vol. 5, no. 6, pp. 773–809, 2011.

[4] R. Eymard, T. Gallouët, and R. Herbin, "Finite volume methods," *Handbook of numerical analysis*, vol. 7, pp. 713–1018, 2000.

[5] C.-D. Munz, R. Schneider, and U. Voß, "A finite-volume method for the maxwell equations in the time domain," *SIAM Journal on Scientific Computing*, vol. 22, no. 2, pp. 449–475, 2000.

[6] P. Monk, *Finite element methods for Maxwell's equations*. Oxford University Press, 2003.

[7] A. Mitchell, "Of the finite element method," in *The Mathematics of Finite Elements and Applications: Proceedings of the Brunel University Conference of the Institute of Mathematics and Its Applications Held in April 1972*. Academic Press, 2014, p. 37.

[8] J. Alvarez, L. D. Angulo, M. R. Cabello, A. R. Bretones, and S. G. Garcia, "An analysis of the leap-frog discontinuous galerkin method for maxwell's equations," *IEEE Transactions on Microwave Theory and Techniques*, vol. 62, no. 2, pp. 197–207, 2014.

[9] B. Cockburn and C.-W. Shu, "Runge–kutta discontinuous galerkin methods for convection-dominated problems," *Journal of scientific computing*, vol. 16, no. 3, pp. 173–261, 2001.

[10] D. M. Sullivan, *Electromagnetic simulation using the FDTD method*. John Wiley & Sons, 2013.

[11] A. Taube, M. Dumbser, C.-D. Munz, and R. Schneider, "A high-order discontinuous galerkin method with time-accurate local time stepping for the maxwell equations," *International Journal of Numerical Modelling: Electronic Networks, Devices and Fields*, vol. 22, no. 1, pp. 77–103, 2009.

[12] S. Yan and J.-M. Jin, "A dynamic p-adaptive dgtd algorithm for electromagnetic and multiphysics simulations," *IEEE Transactions on Antennas and Propagation*, vol. 65, no. 5, pp. 2446–2459, 2017.

[13] J. Mi, Q. Ren, and D. Su, "Parallel subdomain-level dgtd method with automatic load balancing scheme with tetrahedral and hexahedral elements," *IEEE Transactions on Antennas and Propagation*, vol. 69, no. 4, pp. 2230–2241, 2020.

[14] S. Dosopoulos and J.-F. Lee, "Discontinuous galerkin time domain for maxwell's equations on gpus," in *2010 URSI International Symposium on Electromagnetic Theory*. IEEE, 2010, pp. 989–991.

[15] J.-M. Jin, *The finite element method in electromagnetics*, third edition ed. Hoboken. New Jersey: John Wiley & Sons Inc, 2014.

[16] J. S. Hesthaven and T. Warburton, "Nodal high-order methods on unstructured grids: I. time-domain solution of maxwell's equations," *Journal of Computational Physics*, vol. 181, no. 1, pp. 186–221, 2002.

[17] U. S. Inan and R. A. Marshall, "Numerical electromagnetics: The fdtd method," p. 406.

[18] A. Taflove and S. C. Hagness, *Computational electrodynamics: the finite-difference time-domain method*, 3rd ed., ser. Artech House antennas and propagation library. Boston: Artech House, 2005.

[19] A. Z. Elsherbeni and V. Demir, *The finite-difference time-domain: method for electromagnetics with MATLAB simulations*, 2nd ed., ser. ACES Series on Computaional Electromagnetics and Engineering. Edison, NJ: SciTech Publishing, an imprint of the IET, 2016.

[20] R. F. Harrington, *Time-harmonic electromagnetic fields*, ser. IEEE Press series on electromagnetic wave theory. New York: IEEE Press : Wiley-Interscience, 2001.